

From Doped Coordination Polymer Precursor to Cobalt-Doped ZnO Electrocatalyst for Alkaline Hydrogen Evolution Reaction

Roussin Lontio Fomekong,* Paulin Kammi Yontchoum, Tobie Junior Matemb Ma Ntep, Hypolite Mathias Tedjieukeng Kamta, Patrice Kenfack Tsobnang, Svitlana Krüger, Jiří Šturala, Zdenek Sofer, Christoph Janiak, Bilge Saruhan, Arnaud Delcorte, and John Ngolui Lambi

The large-scale application of water electrolysis, for clean H₂ production, requires the development of eco-friendly and low-cost electrocatalysts with high activity for hydrogen evolution reaction (HER) in alkaline media. The excellent alternatives to the benchmark noble metal-based HER electrocatalyst are transition metal oxides (TMO). Because of the nontoxicity, cost-effectiveness, availability, and easy electronic structure tuning, zinc oxide (ZnO) is a good TMO candidate. However, ZnO shows poor performance for HER electrocatalysis and therefore has been much less reported. Herein, it is reported that ZnO can be developed as a good HER electrocatalyst in alkaline media through simultaneously proper cobalt loading at the precursor level (coordination polymer) and defects engineering. The optimum amount of cobalt in ZnO shows an overpotential of 385 mV at 10 mA cm⁻² (lower than that of ZnO and Co₃O₄) and a small Tafel slope of 76 mV dec⁻¹. The introduction of cobalt at the precursor level and subsequently in the wurtzite frame of ZnO as revealed by the analyses, allows to considerably lower the bandgap and increasing the number of defects in the structure, thereby boosting the electrocatalytic performance. This work highlights the potential of cheap and environmentally friendly TMO as alternative HER electrocatalysts for large-scale alkaline water electrolysis.

1. Introduction

Hydrogen, on account of its high energy density and zero-greenhouse gas emissions, is considered the most promising clean energy vector in decarbonized economies.^[1] Nevertheless, the cost- and energy-effective production of hydrogen is the first critical step toward realizing this gas as a common energy carrier and alternative to fossil fuels.^[2] Low-carbon (“green”) hydrogen is produced from the photovoltaic-powered electrochemical splitting of water, which involves hydrogen evolution reaction (HER) at the cathode and oxygen evolution reaction at the anode. For both half-reactions, a catalyst is required to minimize the overpotential and boost the kinetics of these relatively sluggish processes.^[3] In this respect, the usage of benchmark Pt/Pd-based catalysts toward HER impedes the large-scale industrial implementation of this technology because of the scarcity of these noble metals and the associated huge cost.^[4] There is currently intense research

R. Lontio Fomekong, P. Kammi Yontchoum, H. M. Tedjieukeng Kamta, J. N. Lambi
Higher Teacher Training College
University of Yaounde I
Yaounde P.O. BOX 47, Cameroon
E-mail: roussin.lontio@univ-yaounde1.cm

R. Lontio Fomekong, S. Krüger, B. Saruhan
German Aerospace Center
Institute of Materials Research
Linder Hoehe, Cologne 51147, Germany

 The ORCID identification number(s) for the author(s) of this article can be found under <https://doi.org/10.1002/aesr.202300232>.

© 2023 The Authors. Advanced Energy and Sustainability Research published by Wiley-VCH GmbH. This is an open access article under the terms of the Creative Commons Attribution License, which permits use, distribution and reproduction in any medium, provided the original work is properly cited.

DOI: 10.1002/aesr.202300232

R. Lontio Fomekong, J. Šturala, Z. Sofer
Department of Inorganic Chemistry
University of Chemistry and Technology
Technicka 5, Prague 16628, Czech Republic

R. Lontio Fomekong, A. Delcorte
Institute of Condensed Matter and Nanoscience
Université catholique de Louvain
1 Place Louis Pasteur, Louvain-la-Neuve 1348, Belgium

T. J. Matemb Ma Ntep, C. Janiak
Institut für Anorganische Chemie
Heinrich-Heine-Universität Düsseldorf
Düsseldorf D- 40204, Germany

P. Kenfack Tsobnang
Department of Chemistry
University of Dschang
Dschang P.O. BOX 67, Cameroon

activity to find cheaper alternative non-noble metal-based catalysts to address the cost-effectiveness of HER.^[5] In this context, some progress in recent years has disclosed engineered non-noble *d*-block metal oxides as promising electrocatalyst candidates for HER.^[6] For instance, the normal spinel-type structure, Co₃O₄, in which Co²⁺ and Co³⁺ occupy tetrahedral and octahedral sites, respectively, was reported to allow, when supported by carbon fiber electrode, water splitting at a voltage nearly the same as with commercial Pt/C.^[7] On account of the dynamic interchange of Co³⁺ and Co²⁺, some cobalt (Co)-based electrocatalysts have been reported to even exceed, under certain conditions, the activity of Pt for HER.^[8] However, the limited resources of Co and the associated toxicity make Co-based compounds unlikely to satisfactorily address the cost-related challenge of catalysts for water splitting in the long term.^[9] Meanwhile, zinc oxide (ZnO) as a nontoxic, low-cost, and widely available metal oxide (at large industrial scale) should be an economically ideal catalyst option for HER. ZnO as an n-type semiconductor material, with a bandgap of 3.32 eV, is known for its high electrochemical stability. It is used in sunscreens, UV lasers, chemical gas sensors, solar cells, and photo- and electrocatalysts on account of its good optical, electrical, and piezoelectric properties.^[10] Unfortunately, its catalytic activity toward HER was reported to be very low.^[11] A sound compromise could be to dope the less electroactive ZnO with a small amount of Co, to modify and/or tune the catalytic properties of the former oxide.^[12] Co-doped ZnO, known as a green pigment, has been prepared using a wide variety of routes including solid-state reactions, sol-gel, hydrothermal, coprecipitation, autocombustion, Pechini process, and used for various applications.^[13] However, there is no report, to the best of our knowledge, of Co-doped ZnO as an electrocatalyst for HER under alkaline conditions. It is worth noting that, although most of the early reported catalyzed HER were conducted in acidic media, the HER in real industry situations is often conducted in alkaline media. This is to ensure the durability of the electrolysis unit, despite much slower kinetics compared to when the reaction is conducted in acidic media.^[14]

While doping metal oxides can boost their properties by creating vacancies/defects and improving charge mobility, the effectiveness of doping depends on the implemented preparation method.^[15] Besides other preparation routes to complex metal oxides, that is, doped or mixed-metal oxides, the use of a single source precursors (SSPs) route enables to define and control the stoichiometry and the homogeneity at the molecular level, as well as yields complex metal oxides at relatively low temperatures.^[16] In this regard, coordination polymers (CPs) or metal-organic frameworks (MOFs) are appealing SSP candidates due to their modular construction.^[17] CPs are made up of polytopic organic ligands (linkers) which connect metal or metal-containing clusters (nodes), hence forming a well-ordered network.^[18] It is possible to form mixed-metal networks into which all the required metals are incorporated into a single precursor in a highly ordered manner.^[19] This strategy has been employed by some research groups to prepare metal-doped CPs and MOFs, which were thermally decomposed to afford corresponding doped metal oxides under the retention of the particles shape of the precursor materials.^[20]

Herein, Co-doped Zn-based CPs are easily synthesized for the first time at room temperature, within a few minutes in ethanol, using inexpensive succinic acid as the linker and used as a precursor for Co-doped ZnO synthesis. Alongside the two-reference Zn succinate (ZnSuc) and Co succinate (CoSuc) CPs, four Co doping concentrations of 2, 4, 8, and 16 mol% of the ZnSuc are prepared. Remarkably, the doping process is nicely monitored by the color variation of the corresponding CPs, relative to the type of coordination environment of the Co atom. The resulting doped CPs are used as SSPs to afford the targeted Co-doped ZnO s (Co_xZn_{1-x}O; *x* = 0.02, 0.04, 0.08, 0.16) via pyrolysis, which are then thoroughly characterized and evaluated as electrocatalysts for HER in alkaline solution.

2. Results and Discussion

2.1. Characterization of Materials

2.1.1. Succinate-Based Zn and Co CP Precursors

The reaction of succinic acid with ZnCO₃, or CoCO₃, yielded white and pink-colored powder materials which were denoted as ZnSuc and CoSuc, respectively. The powder X-ray diffraction (PXRD) patterns of the materials (Figure 1a) reveal that ZnSuc and CoSuc are microcrystalline powders whose phases correspond to previously reported ZnSuc and CoSuc CPs, respectively.^[21] ZnSuc consists of a 3D CP (Figure 2a), [Zn(C₄H₄O₄)], in which each Zn atom is tetrahedrally coordinated by four succinate linkers (Figure 2b). CoSuc is a 1D CP (Figure 2c), [Co(H₂O)₄(C₄H₄O₄)], in which each Co atom is octahedrally coordinated by four equatorial water molecules and two axial succinate linkers (Figure 2d). Interestingly, ZnSuc and CoSuc form readily at room temperature from ethanolic solutions. In addition, the use of metal carbonates in this synthesis route ensures good purity products because water and CO₂ are the sole by-products.

When the reaction was conducted from a presynthesized mixed Co-Zn carbonate, the formed products, surprisingly, featured a violet color which evolved to deep violet, with increasing Co content from 2% to 16% of the total molar metal content. The PXRD patterns of the materials from mixed Co-Zn carbonate display the phase of ZnSuc, except for the apparition of the side phase of CoSuc when the Co content was increased to 8% and then to 16% (Figure 1a). In fact, a 3D CoSuc CP, in whose structure the Co²⁺ cation is tetrahedrally coordinated, was reported to be violet-colored.^[22] This observation indicates the occurrence of doping of ZnSuc, whereby the Co atom isomorphically substitutes some Zn atoms in the 3D framework of ZnSuc. The number of Zn substitutions increases with the amount of Co content, thereby displaying darker coloring. In the infrared spectra of both ZnSuc and CoSuc (Figure 1b), the bands at about 1520 and 1380 cm⁻¹ correspond, respectively, to the asymmetric and symmetric stretching vibrations of coordinated carboxylates of the succinate. The lower separation between the asymmetric and symmetric frequencies in ZnSuc ($\Delta = 128$ cm⁻¹) compared to that in CoSuc ($\Delta = 140$ cm⁻¹) is in agreement with a bidentate bridging coordination mode of both carboxylates of the succinate linker, against the unidentate coordination in CoSuc. The

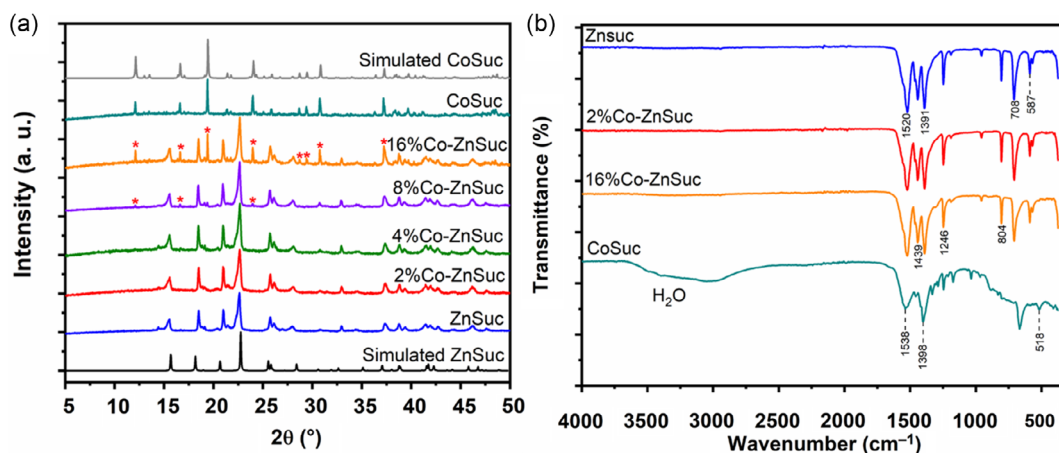


Figure 1. a) PXRD patterns and b) FTIR spectra of pristine ZnSuc, CoSuc, and all the Co-doped Zn succinates.

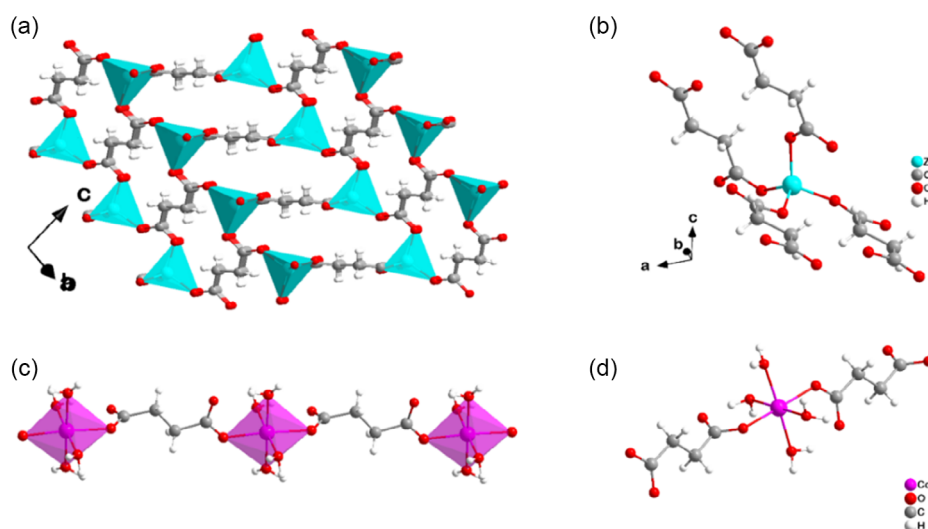


Figure 2. a) 3D packing of ZnSuc framework and b) its crystal structure showing the coordination environment of the Zn²⁺ cation. c) 1D polymeric chain of CoSuc and d) its crystal structure showing the coordination environment of the Co²⁺ cation. Graphics are drawn from CIF files (CSD-Refcode OFUWIV02 and FUMNAC).

difference in their coordination modes is further seen in their Raman spectra (Figure S1a, Supporting Information), where CoSuc features a single band at 1431 cm^{-1} , ascribed to the stretching vibration of the unidentately (*syn*-)coordinated $-\text{COO}$. Meanwhile, two bands are observed at 1467 and 1407 cm^{-1} in the Raman spectrum of ZnSuc. These are ascribed to stretching vibrations of *anti-syn* coordinated $-\text{COO}$. The IR and Raman spectra of Co-doped ZnSuc CPs are identical to that of ZnSuc (see Figure 1b and S1b, Supporting Information), which is in line with the effective doping.

The Co and Zn content was determined by inductively coupled plasma atomic emission spectroscopy (ICP-AES) analysis to reveal six compounds of respective exact formulae $\text{Co}_x\text{Zn}_{1-x}(\text{Suc})\cdot n\text{H}_2\text{O}$ ($x = 0, 0.015, 0.034, 0.08, 0.16, 1$; Suc = succinate dianion) (see Table S1, Supporting Information).

Figure 3 shows the results obtained from the time-of-flight secondary ion mass spectrometry (ToF-SIMS) analysis to confirm the substitution of Zn by Co in the ZnSuc CP. The positive mass spectra presented in the appropriate m/z range exhibit for ZnSuc (Figure 3a), the peaks at $127.8, 131.8,$ and 135.8 u correspond to Zn_2^+ (i.e., ionized cluster ZnZn^+ not ion Zn^{2+}) in the expected isotopic ratio, and for CoSuc (Figure 3d), the peak at 117.8 corresponds to Co_2^+ . Interestingly, in the 2% Co-ZnSuc (Figure 3b) and 16% Co-ZnSuc (Figure 3c) mass spectra, in addition to the presence of both Zn_2^+ and Co_2^+ separately, new peaks emerge around $122.8, 124.8,$ and 126.8 u attributed to ZnCo^+ in the expected Zn isotopic ratio. The ZnCo^+ and Co_2^+ intensities increase whereas Zn_2^+ decreases with increasing amounts of Co. As reported in the literature, in SIMS, $10\text{--}30\text{ Bi}_{3-5}^+$ primary ions eject matter from a hemispherical crater that is smaller than 10 nm in width.^[23] In the case of 2% Co-ZnSuc

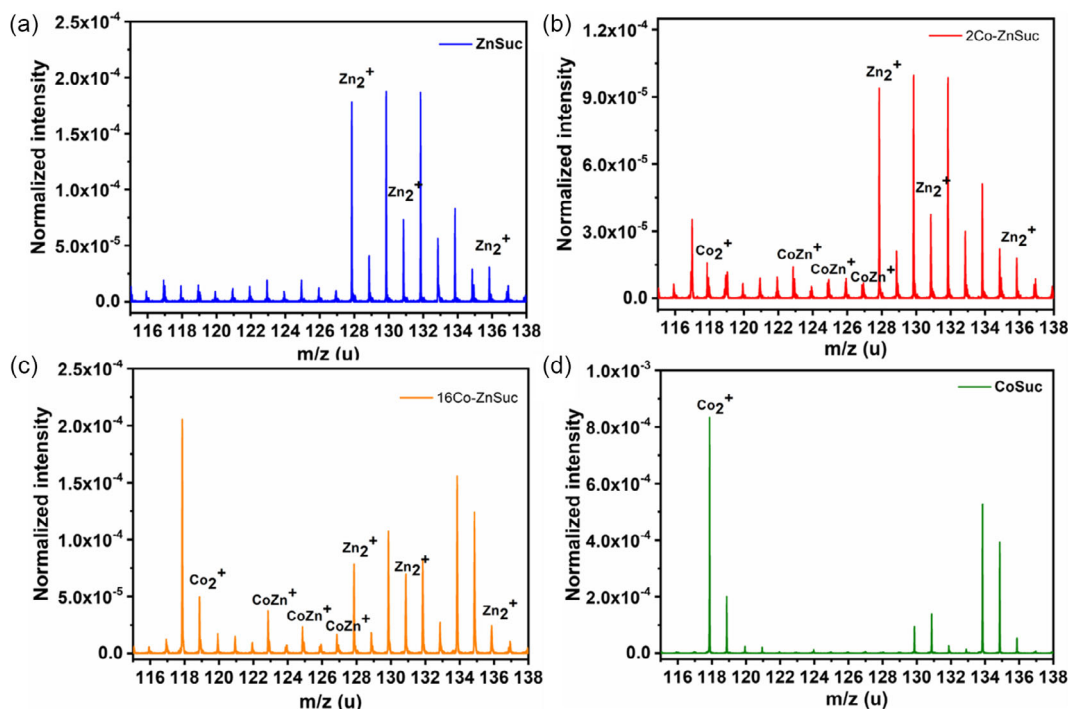


Figure 3. Partial positive ToF-SIMS spectra of a) ZnSuc, b) 2% Co–ZnSuc, c) 16% Co–ZnSuc, and d) CoSuc showing the Co_2^+ , CoZn^+ , and Zn_2^+ peak isotopes. The peak intensities are normalized with respect to the total spectrum intensity (total counts).

and 16% Co–ZnSuc, the particle sizes are far more than 10 nm, such that the presence of intense ZnCo^+ peaks indicates colocalization of Co and Zn at the atomic scale and in the same particle. This should be due to the substitution of Zn by Co in the ZnSuc in agreement with the XRD results reported above.

In view of using the Co-doped Zn succinates as molecular single-source precursors for the production of Co-doped ZnO, their thermogravimetric analysis (TGA) was conducted under synthetic air (Figure S2a, Supporting Information). The thermogravimetric (TG) curves reveal that all the materials decompose at a temperature below 500 °C. Remarkably, the TG trace of ZnSuc displays a single weight loss, at 450 °C, associated with the decomposition of the organic moiety. No step attributable to the release of solvent/ H_2O molecules from its structure is present. This agrees with its anhydrous nature as seen in the unit formula $[\text{Zn}(\text{C}_4\text{H}_4\text{O}_4)]$, which is corroborated by the absence in the infrared spectrum of any band at about 3400 cm^{-1} , which would be attributable to the stretching vibrations of water molecules. However, the TG trace of CoSuc features a weight loss at 100 °C, which is attributable to the release of water molecules from the structure. This can be explained by the presence of four coordinated water molecules per unit formula (29% calculated vs 24% experimental from the TGA data). The presence of water is confirmed by the broadband at about 3400 cm^{-1} in the infrared spectrum, which is ascribed to the stretching vibrations of water molecules. The 2% and 4% Co-doped ZnSuc show a single weight loss, which is, however, shifted to 420 and 437 °C, respectively. All the other doped ZnSuc show two main weight losses associated with the decomposition of CoSuc and ZnSuc, respectively. However, the position of the step is slightly shifted with

respect to those of pristine CPs, as clearly revealed by different temperature positions of decomposition heat peaks in their differential scanning calorimetry (DSC) curves (Figure S2b, Supporting Information). These indicate that at 2% and 4% Co doping, the Co atom completely substituted Zn atoms in the structure of ZnSuc, while there is simultaneous Zn substitution and side phase formation of CoSuc for the other doping percentage, resulting in a complex composite. The results from the TGA are in good agreement with those observed from the PXRD analysis.

2.1.2. Simple and Co-Doped ZnO from Thermal Decomposition of CPs

The residues obtained after the thermal decomposition of all the precursors (ZnSuc, CoSuc, 2% Co–ZnSuc, 4% Co–ZnSuc, 8% Co–ZnSuc, and 16% Co–ZnSuc) were identified by PXRD and the results are presented in Figure 4a. The diffractograms obtained from the thermal decomposition residues of ZnSuc and CoSuc can be assigned to the pure hexagonal wurtzite phase of ZnO (JCPDS # 01-076-0704) and cubic phase of Co_3O_4 (JCPDS # 96-900-5890), respectively. However, the residues containing 2, 4, and 8% of Co consist of a single hexagonal wurtzite phase of ZnO while at 16% an additional cubic phase of Co_3O_4 is observed (Figure S3a, Supporting Information). This can be explained by the fact that for the Co amount less or equal to 8%, Co^{2+} cations were incorporated into the ZnO structure by substituting some Zn^{2+} cations, and once the limit of incorporation was reached, the additional Co formed a Co_3O_4 side phase as observed for 16% Co–ZnO. It is worth noting that the

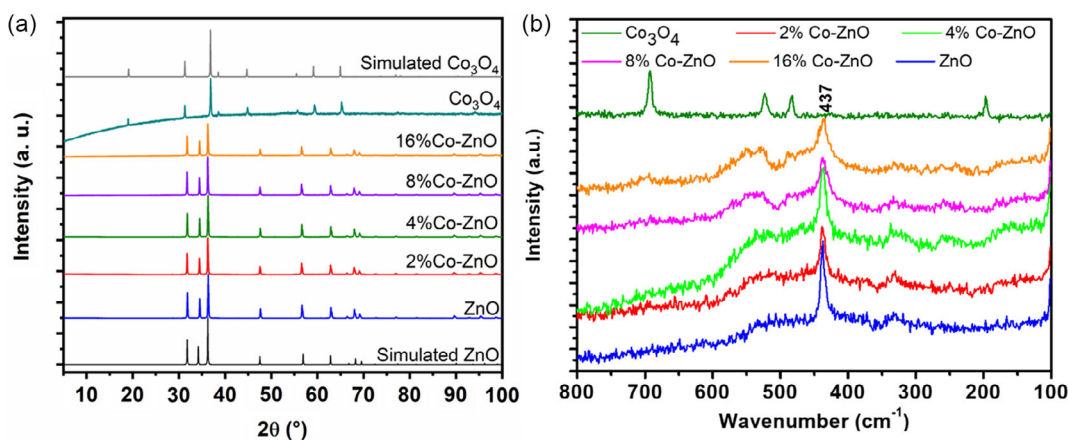


Figure 4. a) PXRD patterns and b) Raman spectra of pristine ZnO, Co_3O_4 , and all the Co-doped ZnO.

incorporation of Co was achieved at the precursors level already, thereby reducing the temperature and the time usually needed to incorporate Co in the structure of ZnO.^[24] From Figure S3b, Supporting Information, it can be observed slight shifts of reflection positions toward lower 2θ angles, indicating the increase of the ZnO lattice parameter with an increasing amount of Co, because the radius of Co^{2+} (79 pm) is slightly greater than that of Zn^{2+} (74 pm) in tetrahedral coordination.

The Raman spectroscopy measurements were performed to further investigate the structure and examine the defects of the prepared materials and the results are shown in Figure 4b. Pristine ZnO shows two bands at 437 cm^{-1} and around 535 cm^{-1} which is associated with E_2 high mode and E_1 symmetry with longitudinal optical (LO) modes, respectively, confirming the formation of ZnO as previously reported in the literature.^[25] The same vibration modes are observed for 2, 4, 8, and 16% Co-ZnO which corroborate the results obtained from PXRD analysis. However, a decrease in intensity is observed at 8% and 16%, suggesting the increase of defects in the structure, probably due to the substitution of Zn by Co. A similar observation was already reported in the literature.^[26] The obvious three bands identified at about 475 , 525 , and 695 cm^{-1} in the spectrum of Co_3O_4 correspond to its Raman-active modes as reported in the literature.^[27] The Raman bands at 475 and 525 cm^{-1} have E_g and F_{2g} symmetry, respectively, while the strong band at 695 cm^{-1} , characteristic of octahedral sites, is attributed to the A_{1g} species in the Oh spectroscopy symmetry.

The UV-vis diffuse reflectance spectra of pristine ZnO, Co_3O_4 , and all the Co-doped ZnO were measured, and the results are depicted in Figure 5a. In the undoped ZnO, no absorption is observed in the visible-light region. However, as the amount of Co increases, the absorbance intensity increases in the visible-light region, displaying three sub-bandgap absorption peaks located around 570, 620, and 660 nm. The position of these three bands corresponds well with the crystal field $d-d^*$ transitions of tetrahedrally coordinated Co^{2+} ions, ${}^4A_2(F) \rightarrow {}^2A_1(G)$, ${}^4A_2(F) \rightarrow {}^4T_1(P)$ and ${}^4A_2(F) \rightarrow {}^2E(G)$, respectively.^[28] As the Zn^{2+} sites in the wurtzite crystal structure have a tetrahedral coordination, the occurrence of three absorption peaks in the visible-light region indicates that the majority of Co ions are

unlikely precipitated as CoO (with hexagonal coordination) or Co metal, but are rather located at the Zn^{2+} sites in the ZnO crystal lattice with the valence state of 2+. Tauc's relation was used to evaluate the bandgap energy of all the samples by extrapolating the linear portion of the plot $(\alpha h\nu)^2$ versus $h\nu$ to the $(\alpha h\nu)^2 = 0$ axis. The results shown in Figure S4, Supporting Information, revealed that the bandgap decreased gradually from 3.01 eV for undoped ZnO to 2.60, 2.50, 2.25, and 2.13 eV for 2, 4, 8, and 16% Co-ZnO, respectively. The bandgap of the pristine Co_3O_4 exhibited a value of 1.45 eV similar to what is already reported in the literature.^[29] This observed redshift in the bandgap of the Co-doped ZnO samples is usually assigned to the $sp-d$ exchange interaction between the localized d -electrons of doping Co ions and the ZnO band electrons lowering the Zn 4s conduction band and raising the O 2p valence band.^[24c] Unlike the redshift observed here, some literature rather reports a blue-shift in the bandgap (which is unfavorable for electrocatalytic applications) after the doping of ZnO by Co, mainly due to the increase of charge carrier resulting certainly from the substitution of Zn^{2+} by Co^{3+} or from the insertion of Co^{2+} .^[30] In this study, the addition of Co at the precursor level led to the easy substitution of Zn^{2+} by Co^{2+} in the ZnSuc CP, avoiding the creation of charge carriers, therefore leading to a redshift which is beneficial for electrochemical applications. This result confirms the possibility of bandgap engineering by suitable control of Co amount at the precursor level.

We performed the X-ray photoelectron spectroscopy (XPS) to provide detailed information about the composition and chemical state of the particles surface. As shown in Figure 5b, the survey spectra reveal the expected main elements (Zn, Co, and O) in the 2% Co-ZnO and 16% Co-ZnO samples. The high-resolution spectra for the two samples (Figure 5c) show the presence of Zn $2p_{3/2}$ lines at 1021.3 eV which could be assigned to Zn^{2+} of ZnO.^[31] The Co $2p_{3/2}$ lines in the two samples (superposed on Figure S5a, Supporting Information) occur at 780.6 eV (2% Co-ZnO) and 779.7 eV (16% Co-ZnO), while the Co $2p_{1/2}$ lines occur at 795.5 eV for both samples (Figure 5d). The small difference observed in the Co $2p_{3/2}$ lines can be ascribed to the difference in the electronegativity of Co and Zn, modifying therefore little bit the chemical environment after doping. All the three

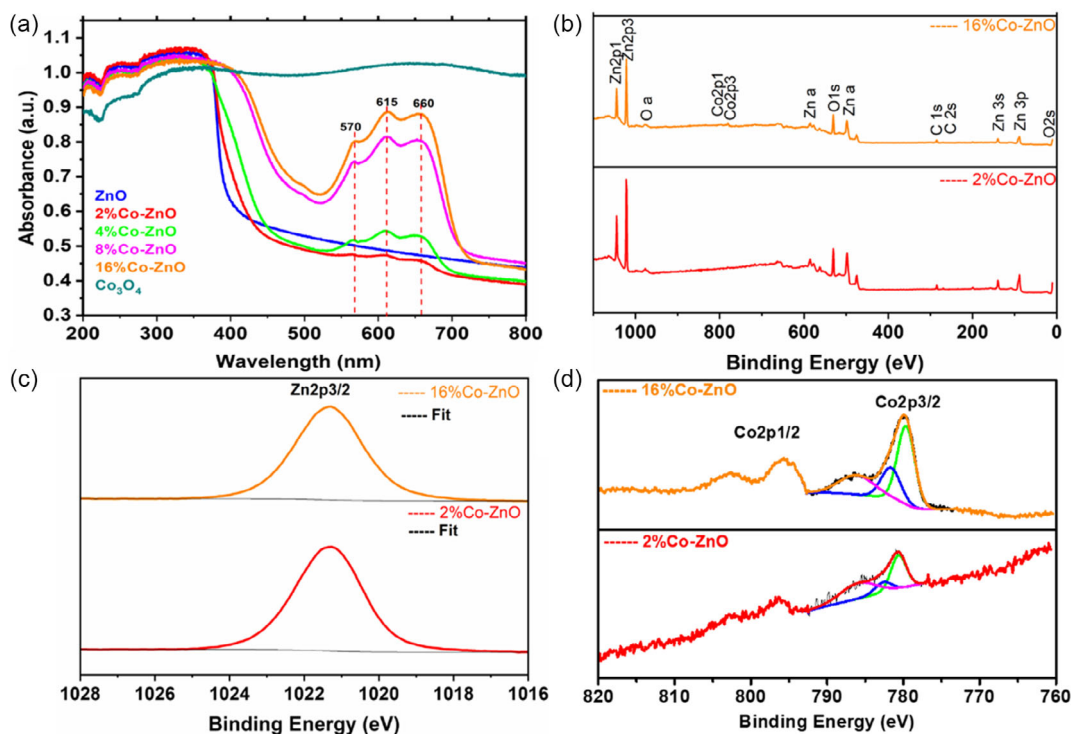


Figure 5. a) UV-vis spectra of all the metal oxides samples, b) survey spectra and high-resolution spectra of c) Zn 2p_{3/2}, d) Co 2p of 2% Co-ZnO and 16% Co-ZnO (Zn a and O a represent the Auger peaks in XPS survey spectrum).

components of the deconvoluted peaks are related to Co²⁺, which fits perfectly with the decomposition model CoO, as reported in the literature.^[32] This was confirmed by the presence of a strong shake-up satellite of Co 2p_{3/2} lines (around 1/2 of the main lines) at 785 eV in 2% Co-ZnO, indicating the presence of mainly Co²⁺ (instead of Co³⁺) as already revealed by the UV-vis diffuse reflectance analysis. However, the decrease of the intensity of that shake-up satellite (around 1/3 of the main lines) in 16% Co-ZnO reveals the presence of the additional Co₃O₄ phase, in accordance with the XRD results.^[33] The XPS spectra of O 1s are presented in Figure S5a, Supporting Information. The shape of the O 1s peaks shows the presence of mainly one component located around 530.4 eV, which is attributable to the lattice oxygen of the ZnO.

Morphologies of all samples were also examined, and the results are presented in Figure 6. The microcrystals of pristine ZnO are elongated polyhedron-shaped with different sizes ranging from 103 to 692 nm while the microcrystals of Co₃O₄ are bipyramidal-shaped and randomly agglomerated. Compared to pristine ZnO, all the Co-doped ZnO samples (excepted 16% Co-ZnO) exhibit almost a similar morphology, with a slight increase of particle size, compared to undoped ZnO. The absence of bipyramidal particles related to Co₃O₄ confirms the presence of only one phase for those doped samples. Energy dispersive x-ray spectroscopy (EDS) spectrum and elemental mapping for 16% Co-ZnO presented in Figure S6, Supporting Information, revealed that Zn and Co are both homogeneously well distributed in the material. The estimated Co/Co + Zn atomic ratio was found to be 0.16 which is in accordance with

the results obtained from ICP-AES where the same ratio was found to be 0.15.

The Fourier-transform infrared (FTIR) spectra of ZnO, Co₃O₄, 2%Co-ZnO, and 16% Co-ZnO (representing all the samples) are presented in Figure S5c, Supporting Information. As it can be observed, no absorption is evident between 3000 and 700 cm⁻¹, indicating that all the organic parts were successfully removed by the thermal treatment. Pristine ZnO and 2% Co-ZnO exhibit the similar spectra with one strong absorption band at 382 cm⁻¹, assigned to the stretching vibration of the Zn-O bond. Co₃O₄ has 2 absorption bands located at 656 and 546 cm⁻¹, corresponding to the stretching vibration of Co-O in the tetrahedral and octahedral sites, respectively. The spectrum of 16%Co-ZnO exhibits a strong absorption band at 376 cm⁻¹, attributed to Zn-O stretching vibrations and a weak absorption band around 656 cm⁻¹, attributed to a small amount of Co₃O₄. This further confirms the formation of a composite material as was already revealed by the XRD analysis.

2.2. Electrocatalytic Performance of Metal Oxides

The catalytic activity of all the pristine (ZnO and Co₃O₄) and doped (Co-doped ZnO) samples including glassy carbon (GC), toward HER, was examined in a 1 M KOH solution. As presented in Figure 7a, the linear scanning voltammetry (LSV) curves reveal that the required overpotential to deliver a current density of 10 mA cm⁻² (η_{10}) for ZnO decreases with the Co feeding amount and are ever lower than that of pristine Co₃O₄ at the highest (16%) amount of Co. As shown in Figure 7b, ZnO and Co₃O₄

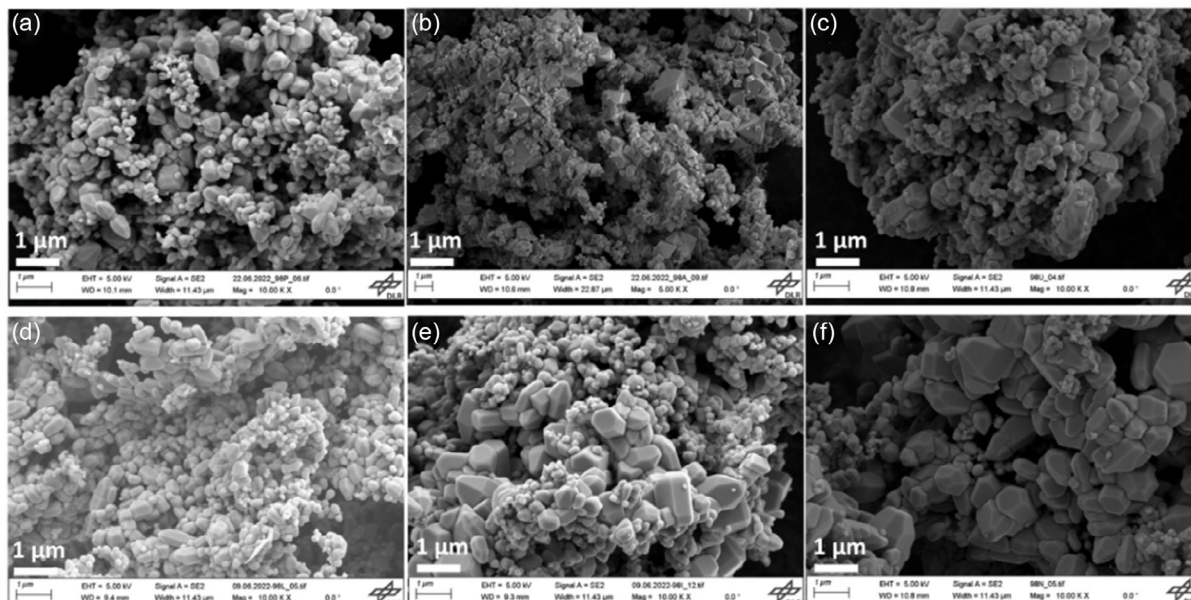


Figure 6. SEM images of a) ZnO, b) Co_3O_4 , c) 2% Co-ZnO, d) 4% Co-ZnO, e) 8% Co-ZnO, and f) 16% Co-ZnO.

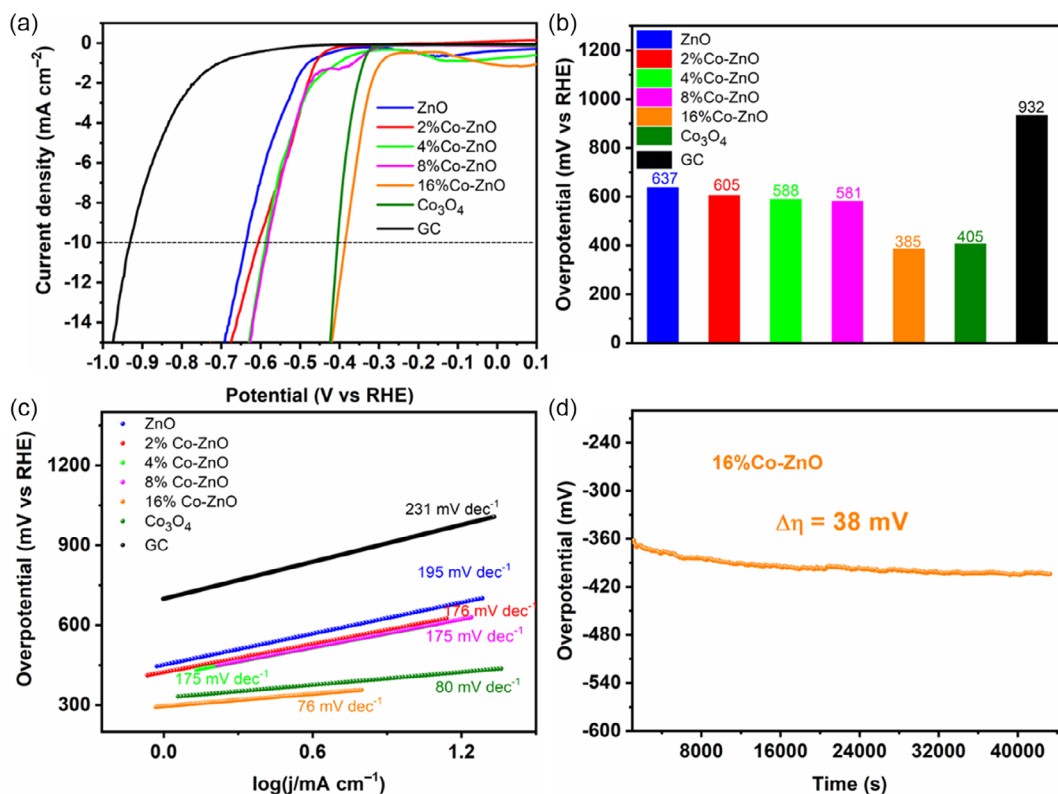


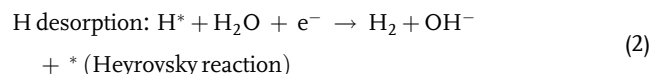
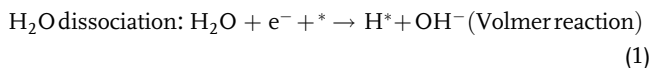
Figure 7. Electrochemical performance for HER in alkaline medium (1 M KOH): a) LSV curves at 2 mV s^{-1} sweep rate, b) overpotential at a current density of 10 mA cm^{-2} , c) Tafel plots obtained from the polarization curves in (a), and d) chronopotentiometry of 16% Co-ZnO.

exhibit the η_{10} values of 637 and 405 mV, respectively, while 2% Co-ZnO, 4% Co-ZnO, 8% Co-ZnO, and 16% Co-ZnO show the η_{10} values of 605, 588, 581, and 385 mV, respectively. 16%

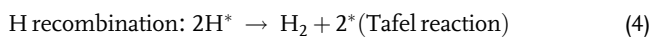
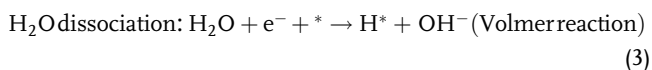
Co-ZnO presents the optimum HER activity among the prepared samples and its η_{10} value is lower than some reported catalysts in the literature.^[34] To further investigate the effect of

Co on HER kinetics, Tafel plots were drawn and presented in Figure 7c. The Tafel slope (TS) calculated shows the values of 195, 176, 175, 175, 76, and 80 mV dec⁻¹ for ZnO, 2% Co-ZnO, 4% Co-ZnO, 8% Co-ZnO, 16% Co-ZnO, and Co₃O₄, respectively. The TS decreases with increasing Co amount and the lowest value recorded for 16% Co-ZnO is eventually lower than many others previously reported in the literature.^[34a,35] In electrocatalysis, the TS value is an important parameter to reveal the HER mechanism. In general, two mechanisms are possible in KOH (where * is the active site of the electrocatalyst).^[36]

Volmer–Heyrovsky mechanism



Volmer–Tafel mechanism



If the TS values are 30, 40, or 120 mV dec⁻¹, the rate-determining steps are Tafel, Heyrovsky, or Volmer reaction, respectively. In this work, all the TS values are higher than 40 mV dec⁻¹, revealing that the rate-determining steps for HER in this study are Heyrovsky or Volmer reaction. However, among the doped samples, as the TS value of 16% Co-ZnO is less than 120 mV dec⁻¹, the rate-determining step is the desorption. This corresponds to the Heyrovsky reaction while for other prepared doped samples, with the TS value being higher than 120 mV dec⁻¹, the rate-determining step is the Volmer reaction.^[37] This suggests that the addition of only 16% of Co in ZnO accelerates the water dissociation step, changing therefore the rate-determining step from the Volmer to the Heyrovsky reaction.

The electrocatalytic performance of the different materials was further evaluated through the double-layer capacitance (*C_{dl}*) obtained from cyclic voltammetry (CV) (Figure S7a, Supporting Information) performed at different scan rates ranging from 10 to 100 mV s⁻¹ in the non-Faradaic region (0.0–0.1 V) and the corresponding electrochemically active surface area (ECSA). Figure S7b, Supporting Information, shows the linear relationship between the current density difference and scan rate at a potential of 0.05 V in a 1 M KOH solution. The *C_{dl}* (and the corresponding ECSA) values of ZnO, 2% Co-ZnO, 4% Co-ZnO, 8% Co-ZnO, 16% Co-ZnO, and Co₃O₄ are 79 μF cm⁻² (1.97), 27 μF cm⁻² (0.68), 49 μF cm⁻² (1.23), 124 μF cm⁻² (3.1), 103 μF cm⁻² (2.60), and 365 μF cm⁻² (9.12), respectively. As it can be observed, at lower amounts of Co (2% and 4%), the *C_{dl}* and ECSA values are lower than that of pristine ZnO, whereas, when a second phase of Co₃O₄ appears (16%), *C_{dl}* and ECSA values increase in accordance with their higher explicit active surface area due certainly to the heterointerfaces between Co-doped ZnO and excess of Co₃O₄.

In order to understand the charge transfer characteristics at the electrolyte/electrocatalyst interface, the electrochemical impedance spectra were measured, and the results are presented in Figure S7c, Supporting Information. Nyquist plots of the bare Co₃O₄ and 16% Co-ZnO exhibited a single semicircle while the pristine, 2% Co-ZnO, 4% Co-ZnO, and 8% Co-ZnO showed complex-plane impedance plots, characterized by two time constants in the form of two well-defined depressed capacitive loops with different sizes. These two capacitive loops participate in the HER kinetics implying that the total charge-transfer resistance (*R_{ct}*) corresponds to the summation of the diameter of the two semicircles. It can be observed that in the selected frequency range and overpotential, the second semicircle exhibited extremely large diameter for 2% Co-ZnO, 4% Co-ZnO, and 8% Co-ZnO, resulting in the large *R_{ct}* while in the Co₃O₄ and 16% Co-ZnO, the *R_{ct}* values are only 89.7 and 108 Ω, respectively. These results indicated that, during the HER process, the transfer of electrons is accelerated in the 16% Co-ZnO, confirming its superior electrocatalytic properties among the other doped ZnO.

The long-term stability of the 16% Co-ZnO was evaluated by performing the chronopotentiometry at a fixed current density of 10 mA cm⁻² for 12 h and the results are presented in Figure 7d. A small drop of 38 mV in the overpotential was observed after 12 h, indicating, therefore, its good stability during the HER process. The cycling performance of the 16% Co-ZnO electrocatalyst was further evaluated by performing the continuous linear sweep voltammogram test. It is seen from Figure S7d, Supporting Information, that a small shift of the overpotential (35 mV) could be observed between the initial polarization curve and the one after 2000 cycles, proving the effective stability of the electrocatalyst for HER in alkaline media.

Table 1 shows several materials that have been reported as electrocatalysts for HER under alkaline conditions. Compared to other electrocatalysts, all the materials synthesized in this work have been obtained easily via a straightforward synthesis route

Table 1. Comparison of the electrocatalytic activity of all the prepared materials with other previously reported for HER in 1 M KOH.

Catalysts	η_{10} [mV]	Tafel slope [mV dec ⁻¹]	Scan rate [mV s ⁻¹]	References
Ce-MnCo ₂ O ₄	389	96	5	[34a]
Fe-NiO/NF	305	105.8	5	[35b]
MoS ₂ /TiO ₂	700	60	5	[34c]
Ag-ZnO	568	192	5	[34b]
Ti ₃ C ₂ T _x /ZIF-8	500	77	5	[39]
NiFe ₂ O ₄	420	133	5	[40]
ZnFe ₂ O ₄	520	144	5	[40]
SrCo _{0.7} Fe _{0.25} Mo _{0.05} O _{3-δ}	323	94	5	[41]
ZnO	637	195		
2% Co-ZnO	605	176		
4% Co-ZnO	588	175	2	This work
8% Co-ZnO	581	175		
Co ₃ O ₄	405	80		
16% Co-ZnO	385	76		

and therefore could be applied at a large scale. Most importantly, the overpotential and TS of 16% Co–ZnO are lower than that of most of the materials reported in Table 1.

As can be observed, among the Co-doped samples, 16% Co–ZnO exhibited the best electrocatalytic performance. The reason behind that may originate from the synthesis process itself. During the preparation, the dopant (Co) is inserted in the main matrix of the ZnSuc CP at the precursor level, therefore optimizing its homogeneous distribution. Moreover, when the insertion limit is reached, the excess of Co forms a second phase, creating a strong heterojunction between Co-doped ZnO and Co₃O₄. Therefore, in the composite material, in addition to the defects created with the substitution of Zn²⁺ by Co²⁺ (as revealed by Raman analysis), additional active sites are created at the hetero-interface of the two components resulting in the enhancement of catalytic activity. In the composite material, the creation of an inner electric field at the p–n interface (Co₃O₄/Co-doped ZnO) can also increase the electron transfer rate, thereby boosting the HER process.^[38] The good stability observed can come from the strong interfacial interaction between Co-doped ZnO and Co₃O₄, granting superior structural integrity in the composite material.

3. Conclusion

In summary, we have succeeded in developing a good, sustainable ZnO-based electrocatalyst thanks to appropriate Co loading right from the precursor level. This was achieved by suitable Co doping of the ZnSuc-based CP, followed by calcination treatment. The optimum amount of Co resulted in a reduced bandgap and an abundance of defects in the prepared materials. This modification endows the material with good electrocatalytic performance in alkaline media, superior to that of pristine ZnO and Co₃O₄. At current densities of 10 mA cm⁻², while pristine ZnO and Co₃O₄ showed overpotentials of 637 and 405 mV, respectively, 16% Co₃O₄ exhibited a low overpotential of 385 mV. The increase in catalytic active sites with the generation of more defects, and the improvement in charge transfer due to the decrease in bandgap, may justify the results observed. Our work provides scientific guidance for stimulating transition metal oxides such as ZnO as a highly active HER electrocatalyst in alkaline media.

4. Experimental Section

Materials for Synthesis: Succinic acid (C₄H₆O₄, 98%, Sigma–Aldrich), cobalt acetate tetrahydrate ((CH₃COO)₂Co·4H₂O, 99%, Merck), zinc acetate dihydrate ((CH₃COO)₂Zn·2H₂O, 99.5%, Merck), potassium hydroxide (KOH, 98%, Sigma–Aldrich), Nafion solution (5%, Merck), ethanol (absolute, Merck), and sodium carbonate (Na₂CO₃, 99%, Merck) were used as received without further purification or processing.

Synthesis of Powder Samples: Pristine ZnO, Co₃O₄, 2, 4, 8%, and 16% Co-doped ZnO denoted as 2% Co–ZnO, 4% Co–ZnO, 8% Co–ZnO, and 16% Co–ZnO, respectively, were prepared following two experimental steps: the synthesis of the precursors (Zn, Co, or Zn–Co succinate) by coprecipitation in ethanolic solution and its subsequent decomposition. ZnSuc, CoSuc, 2% Co-doped ZnSuc (2% Co–ZnSuc), 4% Co-doped ZnSuc (4% Co–ZnSuc), 8% Co-doped ZnSuc (8% Co–ZnSuc), and 16% Co-doped ZnSuc (16% Co–ZnSuc) were all prepared by the same process. Using 2% Co–ZnSuc precursor as an example, Zn–Co carbonate

was first prepared in aqueous solution by adding sodium carbonate (5 mmol) to aqueous solution containing 5 mmol of metal salts including Zn acetate (1.717 g) and Co acetate (0.039 g), in the desired ratio. The resulting precipitate was filtered, dried, and poured slowly in 5 mmol of succinic acid previously dissolved in ethanol. The obtained violet solution was stirred for 90 min, and the precipitate formed was filtered, washed with ethanol to ensure the total removal of impurities, and dried at room temperature to obtain the desired precursor. The as-prepared precursor powder (0.5 g) was calcined in a ceramic combustion boat holder at 550 °C in a muffle oven (10 °C min⁻¹) for 1 h under air flow.

Material Characterization: PXRD patterns were recorded for all the prepared samples on Bruker D8 Advance diffractometer (Bruker, Germany) equipped with a Cu K α ($\lambda = 1.5406 \text{ \AA}$) source. The measurements were done with a step size of 0.05° in the 2θ range of 5–50° for precursors and 5–100° for metal oxide. The Raman spectra were measured with a Raman spectrophotometer from Renishaw using a 532 nm laser, 50x magnification objective, and 1 mW laser power. FTIR spectra were recorded on a Nicolet 6700 FTIR at room temperature, in the spectral range from 4000 to 300 cm⁻¹ for precursors and from 3500 to 300 cm⁻¹ for metal oxides with a resolution of 4 cm⁻¹. The thermal behavior of the precursors was investigated by TGA using Themys TGA (SETARAM instrument). The experiments were performed at a temperature range between 25 and 800 °C, with a heating rate of 10 °C min⁻¹, and in synthetic air as carrier gas with a flow rate of 50 mL min⁻¹. Thermo Jarrell Ash Iris Advantage apparatus was used to perform metal elemental analysis of the precursors via ICP-AES.

The substitution of Zn by Co in the structure of ZnSuc was confirmed using ToF-SIMS on an IONTOF V spectrometer (IONTOF GmbH, Munster, Germany). The investigated samples (ZnSuc, CoSuc, 2% Co–ZnSuc, and 16%Co-ZnSuc) were initially bombarded with Bi₃⁺ ions (30 keV, 45°) and the resulting secondary ions accelerated at 2 kV before entering the analyzer and postaccelerated at 10 kV before detection.

Scanning electron microscopic (SEM) analysis was carried out in a Zeiss Ultra 55 microscope (Zeiss, Jena, Germany). Before the analysis, the samples were sputtered with platinum particles to avoid the charge effect. The optical properties of the samples were investigated using a Jasco V750 UV–vis spectrophotometer (Jasco, Japan) equipped with an integrating sphere, in absorbance mode. XPS using a Kratos Axis Ultra spectrometer (Kratos Analytical, Manchester, UK) equipped with a monochromatized aluminum X-ray source (powered at 10 mA and 15 kV) and an eight-channeltron detector was used to investigate the composition and the chemical state of the various constituents of the as-prepared metal oxides.

Electrochemistry: PGSTAT 204 electrochemical workstation (Utrecht, The Netherlands, NOVA Version 2.1.4) was used to perform at room temperature, the electrochemical HER measurements via a three-electrode system. Ag/AgCl was used as reference electrode, carbon rod as the counter electrode, and GC coated with our materials as the working electrode. The working electrode was prepared by drop-casting 40 μ L onto GC, the as-prepared suspension containing 0.12 mg of active materials followed by drying. A drop of Nafion solution (5 wt%) was deposited on top of the catalyst and dried at 60 °C for 2 h. The measured potentials were recalculated against a reversible hydrogen electrode (RHE) according to the Nernst equation: $E_{\text{RHE}} = E_{\text{Ag/AgCl}} + 0.197 + 0.059 \text{ pH}$, where 0.197 V corresponds to the potential of the reference electrode in 0 pH. The measurement of the LSV in 1 M KOH (pH = 14) with a scan rate of 2 mV s⁻¹ was performed. From the LSV, the overpotential was evaluated using the following equation $\eta = 0 - E$ (vs RHE (V)) and the TS was calculated using the equation $\eta = a + b \log|j|$, with η , a , b , and j corresponding to overpotential, Tafel constant, TS, and current density, respectively. The stability of the best material was investigated by chronopotentiometry for 12 h. CV of all the samples was measured in the potential range from 0.0 to 0.1 V at different scan rates and the electrical double layer capacitances (C_{dl}) were calculated at 0.05 V, by applying the formula, $C_{\text{dl}} = (j_a + |j_c|)/2\nu$, in which j_a and j_c are the anodic and cathodic current density, respectively, and ν is the scan rate. ECSA was measured from non-Faradic capacitive current connected with electrochemical double-layer capacitance (C_{dl}) values obtained from the formula $\text{ECSA} = C_{\text{dl}}/C_s$, where

C_s is the specific capacitance of an automatically smooth planer surface in the respective electrolytic medium. For simple mathematical calculations, the area-normalized specific capacitance was considered to be $40 \mu\text{F cm}^{-2}$ in 1 M KOH.

Supporting Information

Supporting Information is available from the Wiley Online Library or from the author.

Acknowledgements

R.L.F. was supported by ARES-CCD Postdoctoral Fellowship. He also thanks the European Structural and Investment Funds, OP RDE-funded project "CHEMFELLS IV" (grant no. CZ.02.2.69/0.0/0.0/20_079/0017899), DAAD Material Resources Programme for Institutions of Higher Education in Developing Countries and DLR- DAAD Senior Scientist Programme. The authors also thank Pierre Eloy and Claude Poleunis for XPS and ToF-SIMS analyses, respectively.

Conflict of Interest

The authors declare no conflict of interest.

Data Availability Statement

The data that support the findings of this study are available from the corresponding author upon reasonable request.

Keywords

alkaline electrocatalysis, cobalt-doped zinc oxide, coprecipitation, doped coordination polymers, hydrogen evolution reaction

Received: October 23, 2023

Revised: December 4, 2023

Published online:

- [1] J. O. Abe, A. P. I. Popoola, E. Ajenifuja, O. M. Popoola, *Int. J. Hydrogen Energy* **2019**, *44*, 15072.
- [2] T. Terlouw, C. Bauer, R. McKenna, M. Mazzotti, *Energy Environ. Sci.* **2022**, *15*, 3583.
- [3] a) S. Wang, A. Lu, C. J. Zhong, *Nano Convergence* **2021**, *8*, 4; b) S. Shiva Kumar, V. Himabindu, *Mater. Sci. Energy Technol.* **2019**, *2*, 442; c) S. A. Grigoriev, P. Millet, V. N. Fateev, *J. Power Sources* **2008**, *177*, 281.
- [4] S. Sarkar, S. C. Peter, *Inorg. Chem. Front.* **2018**, *5*, 2060.
- [5] a) M. A. Khan, H. Zhao, W. Zou, Z. Chen, W. Cao, J. Fang, J. Xu, L. Zhang, J. Zhang, *Electrochem. Energy Rev.* **2018**, *1*, 483; b) H. Wu, C. Feng, L. Zhang, J. Zhang, D. P. Wilkinson, *Electrochem. Energy Rev.* **2021**, *4*, 473; c) M. Patel, K. K. Joshi, K. H. Modi, P. M. Pataniya, S. Siraj, P. Sahatiya, C. K. Sumesh, *Electrochim. Acta* **2023**, *441*, 141740; d) P. M. Pataniya, V. Patel, P. Sahatiya, D. J. Late, C. K. Sumesh, *Surf. Interfaces* **2022**, *34*, 102319; e) K. K. Joshi, P. M. Pataniya, G. R. Bhadu, C. K. Sumesh, *Int. J. Hydrogen Energy* **2023**, *48*, 7260.
- [6] Y. Zhu, Q. Lin, Y. Zhong, H. A. Tahini, Z. Shao, H. Wang, *Energy Environ. Sci.* **2020**, *13*, 3361.
- [7] S. Du, Z. Ren, J. Zhang, J. Wu, W. Xi, J. Zhu, H. Fu, *Chem. Commun.* **2015**, *51*, 8066.
- [8] a) W. Zhang, L. Cui, J. Liu, *J. Alloys Compd.* **2020**, *821*, 153542; b) Y. Wu, R. Sun, J. Cen, *Front. Chem.* **2020**, *8*, 386; c) J. Ampurdanés, M. Chourashiya, A. Urakawa, *Catal. Today* **2019**, *336*, 161; d) R. Sun, X. Huang, J. Jiang, W. Xu, S. Zhou, Y. Wei, M. Li, Y. Chen, S. Han, *Dalton Trans.* **2022**, *51*, 15205.
- [9] S. Horn, A. G. Gunn, E. Petavratzi, R. A. Shaw, P. Eilu, T. Törmänen, T. Bjerkgård, J. S. Sandstad, E. Jonsson, S. Kountourelis, F. Wall, *Ore Geol. Rev.* **2021**, *130*, 103915.
- [10] a) C. Klingshirm, *Chemphyschem* **2007**, *8*, 782; b) R. Lontio Fomekong, D. Lahem, M. Debliqy, S. Yunus, J. Lambi Ngolui, A. Delcorte, *Sens. Actuators, B* **2016**, *231*, 520; c) S. Raha, M. Ahmaruzzaman, *Nanoscale Adv.* **2022**, *4*, 1868.
- [11] V. M. Sofianos, J. Lee, D. S. Silvester, P. K. Samanta, M. Paskevicius, N. J. English, C. E. Buckley, *J. Energy Chem.* **2021**, *56*, 162.
- [12] a) D. S. A. Pratama, A. Haryanto, C. W. Lee, *Front. Chem.* **2023**, *11*, 1141361; b) A. H. Al-Naggar, N. M. Shinde, J.-S. Kim, R. S. Mane, *Coord. Chem. Rev.* **2023**, *474*, 214864.
- [13] a) N. Zhou, Y. Zhang, S. Nian, W. Li, J. Li, W. Cao, Z. Wu, *J. Alloys Compd.* **2017**, *711*, 406; b) S. Pearton, *Nanoscale* **2010**, *2*, 1057; c) V. Gandhi, R. Ganesan, H. H. Abdulrahman Syedahamed, M. Thaiyan, *J. Phys. Chem. C* **2014**, *118*, 9715.
- [14] a) Y. Zheng, Y. Jiao, A. Vasileff, S. Z. Qiao, *Angew. Chem., Int. Ed. Engl.* **2018**, *57*, 7568; b) M. Đurovič, J. Hnát, K. Bouzek, *J. Power Sources* **2021**, *493*, 229708; c) J. Wei, M. Zhou, A. Long, Y. Xue, H. Liao, C. Wei, Z. J. Xu, *Nano-Micro Lett.* **2018**, *10*, 75.
- [15] T. Gatti, F. Lamberti, R. Mazzaro, I. Kriegel, D. Schlettwein, F. Enrichi, N. Lago, E. Di Maria, G. Meneghesso, A. Vomiero, S. Gross, *Adv. Energy Mater.* **2021**, *11*, 2101041.
- [16] H. Lu, D. S. Wright, S. D. Pike, *Chem. Commun.* **2020**, *56*, 854.
- [17] L. Oar-Arteta, T. Wezendonk, X. Sun, F. Kapteijn, J. Gascon, *Mater. Chem. Front.* **2017**, *1*, 1709.
- [18] a) H. Furukawa, K. E. Cordova, M. O'Keeffe, O. M. Yaghi, *Science* **2013**, *341*, 1230444; b) C. Janiak, J. K. Vieth, *New J. Chem.* **2010**, *34*, 2366.
- [19] a) S. Abednatanzi, P. Gohari Derakhshandeh, H. Depauw, F. X. Coudert, H. Vrielinck, P. Van Der Voort, K. Leus, *Chem. Soc. Rev.* **2019**, *48*, 2535; b) Y. Yang, K. Z. Wang, D. Yan, *Chem. Commun.* **2017**, *53*, 7752.
- [20] a) Y. Song, X. Li, L. Sun, L. Wang, *RSC Adv.* **2015**, *5*, 7267; b) R. Das, P. Pachfule, R. Banerjee, P. Poddar, *Nanoscale* **2012**, *4*, 591; c) R. R. Salunkhe, Y. V. Kaneti, Y. Yamauchi, *ACS Nano* **2017**, *11*, 5293; d) T. Demars, M. Boltoeva, N. Vigier, J. Maynadié, J. Ravaux, C. Genre, D. Meyer, *Eur. J. Inorg. Chem.* **2012**, *2012*, 3875.
- [21] a) T. A. Bowden, H. L. Milton, A. M. Z. Slawin, P. Lightfoot, *Dalton Trans.* **2003**, *5*, 936; b) Y.-Q. Zheng, J.-L. Lin, Z. Kristallogr., *NCS* **2000**, *215*, 159.
- [22] S. Demir, G. K. Kantar, Y. Topcu, Q. Li, *Transition Met. Chem.* **2012**, *37*, 257.
- [23] G. B. Deacon, R. J. Phillips, *Coord. Chem. Rev.* **1980**, *33*, 227.
- [24] a) H. Yang, S. Nie, *Mater. Chem. Phys.* **2009**, *114*, 279; b) O. A. Zelekew, S. G. Aragaw, F. K. Sabir, D. M. Andoshe, A. D. Duma, D.-H. Kuo, X. Chen, T. D. Desissa, B. B. Tesfamariam, G. B. Feyisa, H. Abdullah, E. T. Bekele, F. G. Aga, *Mater. Res. Express* **2021**, *8*, 025010; c) M. Shatnawi, A. M. Alsmadi, I. Bsoul, B. Salameh, G. A. Alna'washi, F. Al-Dweri, F. El Akkad, *J. Alloys Compd.* **2016**, *655*, 244.
- [25] A. Phuruangrat, O. Yayapao, T. Thongtem, S. Thongtem, *J. Nanomaterials* **2014**, *2014*, 1.
- [26] R. Lontio Fomekong, S. You, R. Frohnhoven, T. Ludwig, S. Mathur, B. Saruhan, *Sens. Actuators, B* **2021**, *338*, 129848.
- [27] S. Farhadi, M. Javanmard, G. Nadri, *Acta Chim. Slov.* **2016**, *335*.

- [28] R. He, B. Tang, C. Ton-That, M. Phillips, T. Tsuzuki, J. *Nanopart. Res.* **2013**, *15*, 1.
- [29] L. Qiao, H. Y. Xiao, H. M. Meyer, J. N. Sun, C. M. Rouleau, A. A. Poretzky, D. B. Geohegan, I. N. Ivanov, M. Yoon, W. J. Weber, M. D. Biegalski, *J. Mater. Chem. C* **2013**, *1*, 4628.
- [30] a) A. Chanda, S. Gupta, M. Vasundhara, S. R. Joshi, G. R. Mutta, J. Singh, *RSC Adv.* **2017**, *7*, 50527; b) T. M. Hammad, J. K. Salem, R. G. Harrison, *Appl. Nanosci.* **2012**, *3*, 133.
- [31] R. Lontio Fomekong, H. M. Tedjieukeng Kamta, J. Ngolui Lambi, D. Lahem, P. Eloy, M. Debliquy, A. Delcorte, *J. Alloys Compd.* **2018**, *731*, 1188.
- [32] C. Mark Biesingera, B. P. Paynec, P. A. Grosvenord, L. W. M. Lau, R. A. Gerson, R. S. C. Smart, *Appl. Surf. Sci.* **2011**, *257*, 2717.
- [33] C. Ngnintedem Yonti, P. Kenfack Tsobnang, R. Lontio Fomekong, F. Devred, E. Mignolet, Y. Larondelle, S. Hermans, A. Delcorte, J. Lambi Ngolui, *Nanomaterials* **2021**, *11*, 2833.
- [34] a) X. Huang, H. Zheng, G. Lu, P. Wang, L. Xing, J. Wang, G. Wang, *ACS Sustainable Chem. Eng.* **2018**, *7*, 1169; b) H. Sun, H. Liu, M. Nie, Z. Zhao, Z. Xue, J. Liao, F. Xue, S. Zhang, M. Wu, T. Gao, *Ceram. Int.* **2021**, *47*, 13994; c) A. Tahira, Z. H. Ibupoto, R. Mazzaro, S. You, V. Morandi, M. M. Natile, M. Vagin, A. Vomiero, *ACS Appl. Energy Mater.* **2019**, *2*, 2053.
- [35] a) S. Liu, Y. Xu, D. Chanda, L. Tan, R. Xing, X. Li, L. Mao, N. Kazuya, A. Fujishima, *Int. J. Hydrogen Energy* **2020**, *45*, 1697; b) Z. Qiu, Y. Ma, T. Edvinsson, *Nano Energy* **2019**, *66*, 104118; c) T. Yang, Y. Xu, H. Lv, M. Wang, X. Cui, G. Liu, L. Jiang, *ACS Sustainable Chem. Eng.* **2021**, *9*, 13106.
- [36] N. Mahmood, Y. Yao, J. W. Zhang, L. Pan, X. Zhang, J. J. Zou, *Adv. Sci.* **2018**, *5*, 1700464.
- [37] A. Tahira, Z. H. Ibupoto, M. Willander, O. Nur, *Int. J. Hydrogen Energy* **2019**, *44*, 26148.
- [38] Y. Zeng, Z. Cao, J. Liao, H. Liang, B. Wei, X. Xu, H. Xu, J. Zheng, W. Zhu, L. Cavallo, Z. Wang, *Appl. Catal., B* **2021**, *292*, 120160.
- [39] L. P. Hao, A. Hanan, R. Walvekar, M. Khalid, F. Bibi, W. Y. Wong, C. Prakash, *Catalysts* **2023**, *13*, 802.
- [40] H. Belhadj, Y. Messaoudi, M. R. Khelladi, A. Azizi, *Int. J. Hydrogen Energy* **2022**, *47*, 20129.
- [41] Z. Zhang, Y. Chen, Z. Dai, S. Tan, D. Chen, *Electrochim. Acta* **2019**, *312*, 128.